Design and Modeling of the Bearingless Induction Motor

Jiahao Chen*, Eric L. Severson*
*Department of Electrical and Computer Engineering, University of Wisconsin-Madison, Madison, WI 53706 USA

***Abstract*—The bearingless version of the induction motor (IM) has seen little consideration as a high performance, medium to high power motor. This paper investigates and develops design and performance evaluation techniques that are necessary to systematically study and design the bearingless IM. Key differences in the design considerations of the bearingless IM from that of the classical line-fed or inverter-fed IM are first explored and a candidate design (4 poles, 15,000 rpm, 50 kW) is created using a modified analytic design approach. Finite element analysis (FEA) is used to explore the impact of the rotor topology (squirrel cage or pole-specific rotor winding) on the machine performance. It is shown that for low speed designs, the traditionally-used cage rotor can yield acceptable performance. However, the cage rotor is found to not be a workable solution for high speed designs (an example design operated at 500 Hz requires 20% of rated stator current to merely support the shaft weight). Finally, several FEA techniques are proposed and evaluated based on their ability to rapidly and accurately evaluate the bearingless IM design performance. This investigation will provide the necessary foundation for future efforts in designing and optimizing the bearingless IM.**

***Index Terms*—Bearingless motor, induction motor, magnetic suspension, finite element analysis.**

NOMENCLATURE

p, p_s	Number of pole pairs of torque and suspension winding, respectively.
Q_s, Q_r	Number of stator and rotor slots, respectively.
θ, Ω	Mechanical rotor position and speed, respectively.
E_a, E_m	Force error angle and magnitude, respectively.

I. INTRODUCTION

Bearingless motors are electric motors that are capable of producing both torque and lateral forces on their shaft. They are capable of operating as both a motor and magnetic bearing, but without the magnetic bearing hardware–which offers all the benefits of magnetic levitation, while reducing the system cost and complexity associated with magnetic bearings. During the last decade, interest in this technology has been rapidly growing. Induction motors (IMs) are regarded as the "workhorse" of industry due to their robust structure, suitability for harsh environments, low cost components, and extreme reliability. However, this technology has seen only limited consideration as a bearingless motor–with efforts so-far focused on techniques to obtain decoupled suspension control [1], [2] and shaft vibration suppression [3]–[5].

This work was supported by the scholarship from the China Scholarship Council (CSC) under Grant 201806320062. The authors would like to acknowledge the support of the Wisconsin Electric Machines and Power Electronics Consortium (WEMPEC).

The design of the bearingless IM is an inherently complex and challenging task due to the necessity of induced rotor currents for torque production. The magnetic suspension field used for levitation rotates at a different speed than the torque producing field, and thereby potentially induces very large currents into the rotor that degrade the machine efficiency, suspension force capability, and result in thermal challenges. Accurately modeling this phenomenon comes at considerable computation expense, because the induced rotor currents are a transient effect that develop over several electrical periods before reaching steady state. The combination of these items make the bearingless IM exceedingly difficult to design and optimize. This paper systematically investigates and proposes solutions to these challenges.

This paper first reviews the state of literature as applied to the design of a bearingless IM. Next, the paper considers modifications to the classical machine design approach to create an example 15,000 rpm, 50 kW bearingless IM design. The impact of the suspension field on the bar currents of a cage rotor are investigated for the example design and shown to yield prohibitively poor machine performance. This motivates the use of a pole-specific cage rotor, which does not link the suspension field. Computationally efficient modeling techniques are proposed to model a high speed bearingless IM with a pole specific cage rotor. Finally, the accuracy of the proposed techniques are evaluated for 50 random designs and a modified transient model is suggested as being suitable for future efforts in machine optimization.

II. LITERATURE REVIEW ON BEARINGLESS IMS

A. Stator Winding Design

Typical motor winding arrangements that are able to generate the two required magnetic fields can be classified as either a separate winding [6], [7] or a combined winding. Combined windings can be further divided into multi-phase (≥ 5 phases) windings [8]–[11] and DPNV (Dual Purpose No Voltage) windings [12]–[16].

Separated windings use a fixed slot turns ratio for the torque and suspension winding. This reduces the slot area available for the torque producing winding–and thereby reduces the motor's torque density. The combined winding can dynamically allocate the slot space between suspension and torque current because it uses the same coils to produce force and torque, and is hence preferred from a motor performance perspective.

An effective multi-phase winding for a bearingless motor must generate not only the fundamental spatial magneto-

motive force (MMF) but also second-order spatial MMF [17], [18]. As a result, a double layer, short pitch stator winding is used. A previous study [2] has shown that by proper selection of the coil pitch, the multi-phase winding can achieve lower stator copper loss per MMF than that of a separate winding.

The distinguishing feature of the DPNV winding is that the suspension current path has no back electromotive force (EMF). DPNV windings can be connected as bridge [12], [13] or parallel configurations [15], [19]. A detailed FEA modeling study of a bearingless squirrel cage IM with a bridge DPNV winding is reported in [20]. The example bearingless IM designed in this paper has a DPNV winding that can be connected as either a parallel or bridge configuration.

B. Rotor winding Design

The suspension force is controlled by creating a suspension field in the air gap of the machine which rotates at a different speed than the torque producing field. This means that the rotor has an additional slip speed, relative to the suspension field. In a cage rotor design, rotor currents induced by the suspension field cause undesired gain and delay in the suspension forces. For the purpose of suspension, it is better to have no rotor bars at all [21]. While suspension performance issues can be overcome through advanced control techniques, i.e. [1], [2], the additional rotor currents may result in high losses and thermal issues [2], [6]. This is investigated for the example design of this paper in Section III-C. An alternate solution is to use a pole-specific cage rotor winding [22]–[24] or a wound rotor [25], [26], designed so that it does not link the suspension field. However, this approach has the drawback of requiring multi-layer construction of the end ring / windings, which increases the axial length of the rotor [23]. For example, a $Q_r = 36,\ p = 2$ rotor requires 9 layers of end-rings.

Additionally, in a bearingless motor system, the common practice of skewing the rotor has potential to induce axial oscillations. Axial forces are created by the circumferential component of the skewed rotor current path. A solution is proposed in [27] by utilizing two units of bearingless IMs within a bearingless system. In a bearingless system that consists of a 3-DoF (Degrees-of-Freedom) magnetic bearing and a 2-DoF bearingless IM, the magnetic bearing must cancel any problematic axial forces caused by the skewed rotor.

III. Bearingless IM Design

Fundamental aspects of machine design differ for line-fed IMs, inverter-fed IMs, and bearingless IMs. It is helpful to compare design considerations from different perspectives. For example, in classically designed line-fed IMs, the number of rotor slots (Q_r) is carefully chosen to avoid harmful cogging torque, synchronous torque, noise, and vibration [28]. An odd Q_r value results in noisy start-up conditions. In the more recently developed inverter-fed IMs, the design is focused on the small slip region [29], [30] and an odd Q_r can be used to effectively reduce torque ripple. However, significant radial force oscillations are a potential side-effect of using odd Q_r values, making these values undesirable for bearingless IMs.

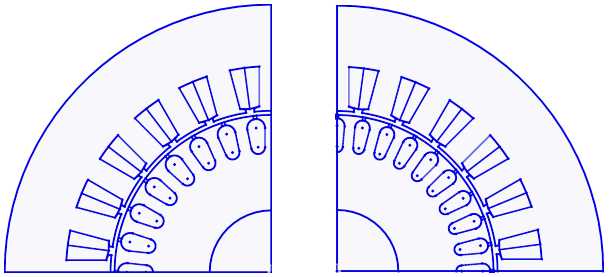

(a) Squirrel cage rotor design with $Q_r = 30$.

(b) Pole-specific rotor design with $Q_r = 36$.

Fig. 1. Cross section views of the candidate bearingless IM designs with $Q_s = 24$, $p = 2$, $p_s = 1$.

A. Specification of Example Design Considered

This paper considers the design of a 50 kW, 500 Hz, four pole motor/two pole suspension, 15,000 rpm, three-phase bearingless IM with a DPNV winding. It is assumed that 2.5% of the slot space is allocated to suspension current and 97.5% of the slot space is allocated to motor current, based on a previous investigation into a 50 kW bearingless permanent magnet motor with a DPNV winding [31], [32]. The cross section views of two candidate IM designs are shown in Fig. 1.

B. Bearingless IM Design Strategy

The bearingless IM design procedure is established by modifying the well-known procedure for AC machines [28]. Mechanical limits are checked for the required rotor diameter and shaft length, as outlined in [28]. The rotor diameter is limited to keep the centrifugal stress on the rotor lamination below the material yield strength and the shaft length is restricted so that the first critical speed is beyond the rated/maximum operation speed.

The equations given in [28] for selecting air gap length δ are only intended for 50 Hz machines, and to avoid excessive iron losses in the stator and rotor teeth, δ has to be increased for high speed motors [28], [33]. However, large δ leads to low power factor and increased stator copper loss. So, the selection of δ is a compromise between these two aspects. This paper increases the "50 Hz δ" by 100%.

The stator voltage is assumed to be 480 Vrms and the winding terminals are wye-connected. To allow a reasonable turns per stator slots, the number of stator slots must be as low as possible, i.e., 12 or 24. This means the distribution factor will have little effect on the 9^{th} and 11^{th}-order harmonic magneto-motive forces (MMFs). This paper uses a design with $Q_s = 24$ slots.

Another empirical design parameter is the number of rotor slots Q_r. Since the choices of Q_r are finite, a study can be performed to compare the influence of different Q_r values. The preferred choices are $Q_r = 16,\ 18,\ 30,\ 32,\ 34,\ 36$ for a squirrel cage rotor [28], and $Q_r = 16,\ 32,\ 36$ for a pole-specific rotor. As a result, there is one main torque ripple component due to slotting that repeats every [34]

$$\frac{360}{2p} \Big/ \text{LCM}\left(\frac{Q_s}{2p}, \frac{Q_r}{2p}\right) \text{ [mech. deg]} \tag{1}$$

where $p = 2$ is the number of pole pairs of the torque winding. This translates into 5 mech. deg for $Q_r = 36$ and leads to 36-th order harmonic in torque profile when the slip is 0. For $Q_r = 30$, (1) gives 1.5 mech. deg, and it corresponds to a 120-th order harmonic (when the slip is 0). Moreover, the $Q_r = 30,\ p = 2$ design will induce no rotor slot harmonic current in the stator winding because the induced EMF cancels each other out [35]. In other words, a squirrel cage rotor can use an even Q_r that is not a multiple of $2p$ to reduce the slot harmonic currents and torque ripple [36], while a pole-specific rotor cannot. In addition, based on FEA simulation, the radial force will have a force ripple component of the same period as predicted by (1).

The slot harmonic MMFs (e.g, of $\frac{Q_s}{p} \pm 1$ and $\frac{Q_r}{p} \pm 1$ th-order) have the same distribution factor as the fundamental [37], hence they must be dealt with by other approaches, e.g., rotor skew. However, slotting effect cannot be eliminated because there are more than one source of rotor slot harmonic current [36]: rotor slot harmonic MMFs interacting with dc air gap permeance, and stator fundamental MMFs interacting with rotor slot permeance harmonics. Proper rotor skew can minimize the former but not the latter [36]. The full effect of rotor skew should be evaluated with voltage source excitation, for it allows stator current harmonics. As mentioned before, the rotor skew causes undesired axial force, so it must be designed along with the bearingless system configuration. Therefore, the rotor skew is preserved for a later stage of the design process and is not considered in this work.

To obtain better thermal performance, the drop shape of rotor slot is adopted in this paper, even though high-speed IMs normally utilize round bar shapes to reduce stress on the lamination [38]. Large rotor slots are suggested for inverter-driven motors in [39]. Therefore, the design procedure is iterated to find the largest possible rotor slot (corresponding to lowest rotor current density) such that the specified magnetic loads at rotor tooth and rotor yoke are satisfied.

C. Selection of Rotor Winding

The cage rotor is easy to manufacture and mechanically robust, and several of the problems caused by induced rotor currents from the suspension winding can be dealt with by control techniques. However, at rated operation, there exist two frequencies of rotor currents: one small slip rotor current created by the torque winding, and one high slip rotor current created by the suspension winding. For high rotational speeds, the high slip current becomes large in amplitude, causing poor efficiency and thermal issues.

To illustrate the impact of rotor currents induced by the suspension winding, an example $p = 2$, $p_s = 1$ cage rotor IM (Fig. 1a) is studied at different rotational speeds. The rotor slip speed (relative to the torque field) and stator current magnitudes are held fixed to produce rated torque and a stationary force vector. Under these conditions, according to the theory of bearingless motors, the suspension winding caries a three phase current at the same frequency as the motor currents [6]. Since the suspension winding has only two poles, it has a field speed that is double that of the motor field speed. As the rotor speed increases, the slip of the rotor relative to the suspension field increases, as shown in Table I, yielding amplitude reduction of the suspension field.

TABLE I
ROTOR SLIP FREQUENCY WITH RESPECT TO DIFFERENT FIELDS (FIG. 2)

Electrical frequency [Hz]	7.5	50	500
Rotor speed [rpm]	0	1275	14775
Rotor speed [s^{-1}]	0	21.25	246.25
4 pole field speed [s^{-1}]	3.75	25	250
2 pole field speed [s^{-1}]	7.5	50	500
4 pole rotor slip freq. [Hz]	7.5^*	7.5^*	7.5^*
2 pole rotor slip freq. [Hz]	$7.5^\dagger$	$28.75^\dagger$	$253.75^\dagger$

*4 pole slip freq. $= p\times$(4 pole field speed $-$ rotor speed).
†2 pole slip freq. $= p_s\times$(2 pole field speed $-$ rotor speed).

Transient 2D FEA calculations performed with JMAG indicate that the suspension force amplitude decreases from 125 N (no rotation) to 8 N (high speed rotation)–shown in the upper-left plot of Fig. 2. The air gap flux density distribution is shown in the right plot of Fig. 2. Since the four-pole field is dominant, the two-pole field can be viewed as the difference between the 1st half (0–180 deg) and the 2nd half (180–360 deg) of the total air gap flux density distribution. The difference decreases as the excitation frequency increases due to the induced currents in the rotor which reduces the suspension force accordingly.

In this example, the rotor weight is 57 N, which suggests that this example bearingless IM with a cage rotor should be designed with a base frequency below 60 Hz to secure a reasonable efficiency (see e.g., [40]). If the excitation is 500 Hz, the candidate cage rotor bearingless IM needs to consume 20% of rated current to support the shaft. Notice in the lower-left plot of Fig. 2 that the torque output is relatively unaffected by the changes in speed and that the design choice to use $Q_r = 30$ has resulted in the expected low amplitude torque ripple, without the use of any skew.

Based on this analysis, to enable a high speed design, the pole-specific rotor winding [24], [41] is adopted in this paper.

IV. MOTOR PERFORMANCE EVALUATION METHODS

This section proposes several FEA based models to analyze the bearingless IM. The goal is to develop a modeling technique that can be linked to a design optimization algorithm. Typical global search algorithms used in electric machine design require the evaluation of hundreds of thousands of candidate designs. This means that the modeling technique must have low computational cost. IMs are notoriously complicated to model due to the startup transients associated with the induced rotor currents. The bearingless IM adds additional computation cost due to its requirement of accurate force calculations, described in Section V.

A. Transient FEA

A high fidelity transient FEA model with a small time-step size is the most accurate method to evaluate the performance of an IM design. Unfortunately, the transient FEA modeling

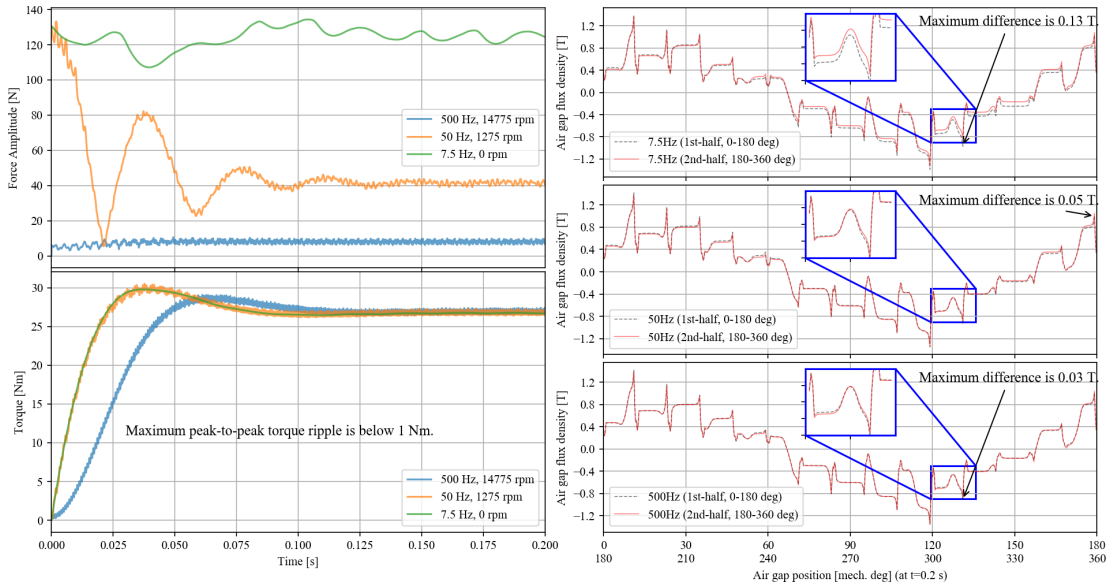

Fig. 2. Force, torque, and flux density distribution (at $t = 0.2$ s) of the example design with a cage rotor for the different rotor speeds indicated in Table I. All cases have a 7.5 Hz slip frequency (relative to the torque field). The slight difference between the first-half (0°–180°) and the second-half (180°–360°) of the four pole torque field is caused by the two pole suspension field used to create forces, which is cancelled at high speeds by induced rotor currents.

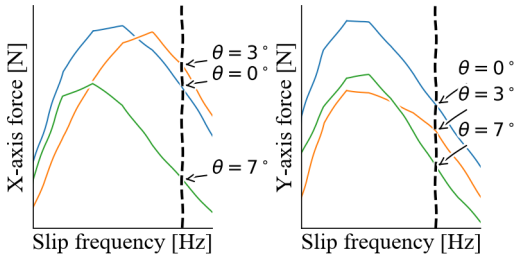

Fig. 3. Illustration of the eddy current FEA technique with a rotating rotor.

approach has far too high of computational expense to be used in the optimization process (an accurate evaluation of a single candidate design requires several hours).

There are several known methods to accelerate transient FEA modeling of an IM, for example [42]–[44] and [45, Sec.2.3]. By using the solution of an eddy current solver as the initial state of a transient FEA, the transient FEA waveforms nearly eliminate the initial transient ("Transient FEA" trace, cf. Fig. 2 and Fig. 5). However, even with these techniques, the solving time is still too long. This is especially true for a high frequency IM, because the maximum time-step size is severely limited by the high stator frequency, while the end-time must be long due to the low slip frequency.

Other modeling methods that are capable of rapid evaluation of torque and force ripple must be developed to enable IM design optimization. The transient modeling technique is treated as the baseline, against which all other modeling techniques explored by this paper are compared.

B. Eddy Current FEA with Rotating Rotor

An alternate approach to IM modeling is to use an eddy current solver where the stator is excited with currents at the slip frequency. The model can be solved for different rotor positions θ to capture the slotting effect [34], which includes the variation in amplitude of the fundamental component of rotor current and the variation in air gap permeance. This paper investigates the accuracy of force ripple calculations using this approach. An illustration of the idea is shown in Fig. 3. Each force–frequency curve is dependent on the rotor position θ. If the slip frequency is fixed, the x- and y-axes force can be calculated as functions of θ.

The results of the eddy current FEA of the example design in the small slip region at 24 different $\theta \in [0, 10]$ mech. deg over one rotor slot pitch are sketched in Fig. 4. The results confirm that the generated torque and force are functions of rotor position. In addition, one notices that the slip of maximum torque is smaller than that of maximum forces.

C. Static FEA with Pre-determined Rotor Current Conditions

Unlike permanent magnetic motors for which a series of static FEA with a rotating rotor can be used to evaluate the torque/force ripple [31], [32], no current will be induced in the rotor bars of an IM in static FEA.

However, static FEA can be used for IM design performance evaluation if the rotor currents are pre-determined from an eddy current FEA solution. The rotor slot currents are extracted from an eddy current solver as complex numbers, which indicate the magnitude and phase of each slot current at the slip frequency as a function of time. For a steady state solution with constant rotor speed Ω, the time is solved by $t = \theta/\Omega$ and the rotor current conditions of the static FEA can be determined for bar n ($n = 1, 2, ..., Q_r$) as (2),

$$\begin{aligned} \bar{I}_n &= \hat{I}_n e^{j\phi_n} \\ \Rightarrow I_n(t) &= \hat{I}_n \cos\left(\omega_{\text{slip}} t + \phi_n\right) \\ \Rightarrow I_n(\theta) &= \hat{I}_n \cos\left(\omega_{\text{slip}} \theta/\Omega + \phi_n\right) \end{aligned} \tag{2}$$

where the slip angular speed is $\omega_{\text{slip}} = \omega_s - p\Omega$ and ω_s is the synchronous angular speed. The performance metrics are

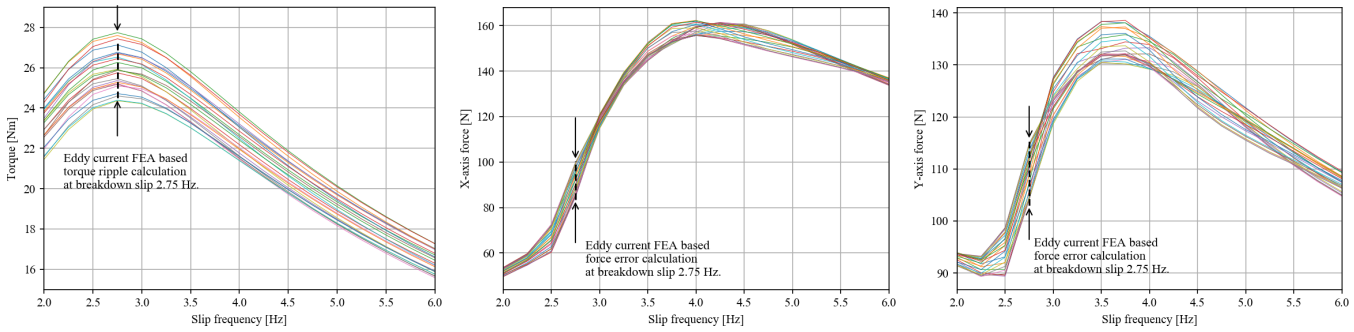

(a) Torque versus frequency (b) X-axis force versus frequency (c) Y-axis force versus frequency

Fig. 4. Results of eddy current FEA in small slip region at 24 different rotor positions over a rotor slot pitch (= 10 mech. deg) for the example design of Fig. 1b. Each line corresponds to different rotor position. Breakdown slip corresponds to the slip at the maximum torque point.

TABLE II
NUMERICAL RESULTS OF THE FEA MODELS FROM FIG. 5

FEA model	**Avg. torque [Nm]**	**Torque ripple [%]**	**Avg. Force [N]**	**Force err. mag. [%]**	**Force err. angle [deg]**
Transient FEA	29.4	4.6	289.3	3.9	2.3
Eddy Current FEA	29.9	3.4	327.7	1.2	0.32
Static FEA	29.1	3.6	278.9	5.1	3.4
Tran. w/ 2 Sections	26.9	5.2	293.6	4.0	2.1

TABLE III
STATISTICAL DATA OF THE 50 RANDOM DESIGNS FROM FIG. 7.

FEA model w/ regular step	**Torque diff. [p.u.]**	**Torque ripple diff. [%]**	**Force mag. diff. [p.u.]**	**Force err. mag. diff. [%]**	**Force err. angle diff. [deg]**
Tran. w/ 2 Sections	$-0.042(9.7\times10^{-5})$*	4.8(24)	0.0068(0.001)	-1(4.2)	-0.52(1.3)
Eddy Current FEA	$0.023(5.1\times10^{-4})$	-6.4(50)	0.09(0.035)	-10(150)	-6.1(75)
Static FEA	$-0.008(2.4\times10^{-4})$	-1.7(22)	-0.01(0.0042)	6.1(39)	4.9(51)

*Note: all statistical data are in the format of "mean(variance)". The FEA model is better if its data are closer to 0.

calculated as a function of θ by evaluating the static FEA model at different $\theta \in [0, 90]$ mech. deg.

One drawback of rotating static FEA is that sliding mesh, which is a key feature in eddy current FEA and transient FEA, cannot be used. As a result, for different rotor positions, the mesh needs to be re-generated, which comes with computation expense. However, static FEA can more easily take advantage of parallel computation.

D. Transient FEA with Two Time Step Sections

Transient FEA with two different time step sections is another potential solution to obtain fast evaluation results. That is, in the first time section, by using a relatively large time step that is still small with respect to slip frequency, the rotor current will reach steady state within a reasonable number of steps (i.e., 32 steps in this paper); in the second time section, small steps with respect to stator frequency are applied in order to evaluate the steady state torque/force ripple. The model is initialized using an eddy current solution as mentioned in Section IV-A to further shorten the start-up transients.

V. VALIDATION OF MOTOR MODELING TECHNIQUES

The bearingless IM models developed in Section IV are now evaluated based on their ability to accurately calculate the following key performance metrics pertaining to torque and force calculation. Other important metrics (efficiency, power factor, and material cost) are not unique to bearingless motors, and are therefore reserved for separate work.

A. Performance Metric Calculations

Torque ripple is calculated as the peak-to-peak value of the torque profile. Force ripple is quantified in terms of a worst case force vector magnitude and angle error that occurs over one rotor revolution [31]. To make a clear definition of the force error angle E_a, an illustration is sketched in Fig. 8. Typical bearingless motor designs minimize force error angle to be within 5° [31], which provides insight into the level of accuracy required of the modeling tool.

Each of the investigated modeling techniques is compared against the reference transient modeling technique described in Section IV-A to determine its accuracy. Comparison quantities are given as either:

1) an absolute difference, for example "force error angle difference [deg]" is calculated as $E_a^{\text{Static}} - E_a^{\text{Ref.Tran.}}$, or
2) a normalized difference, indicated by specifying the difference as per unit "p.u."; for example "force magnitude difference [p.u.]" is calculated as $\frac{|F|^{\text{Static}} - |F|^{\text{Ref.Tran.}}}{|F|^{\text{Ref.Tran.}}}$.

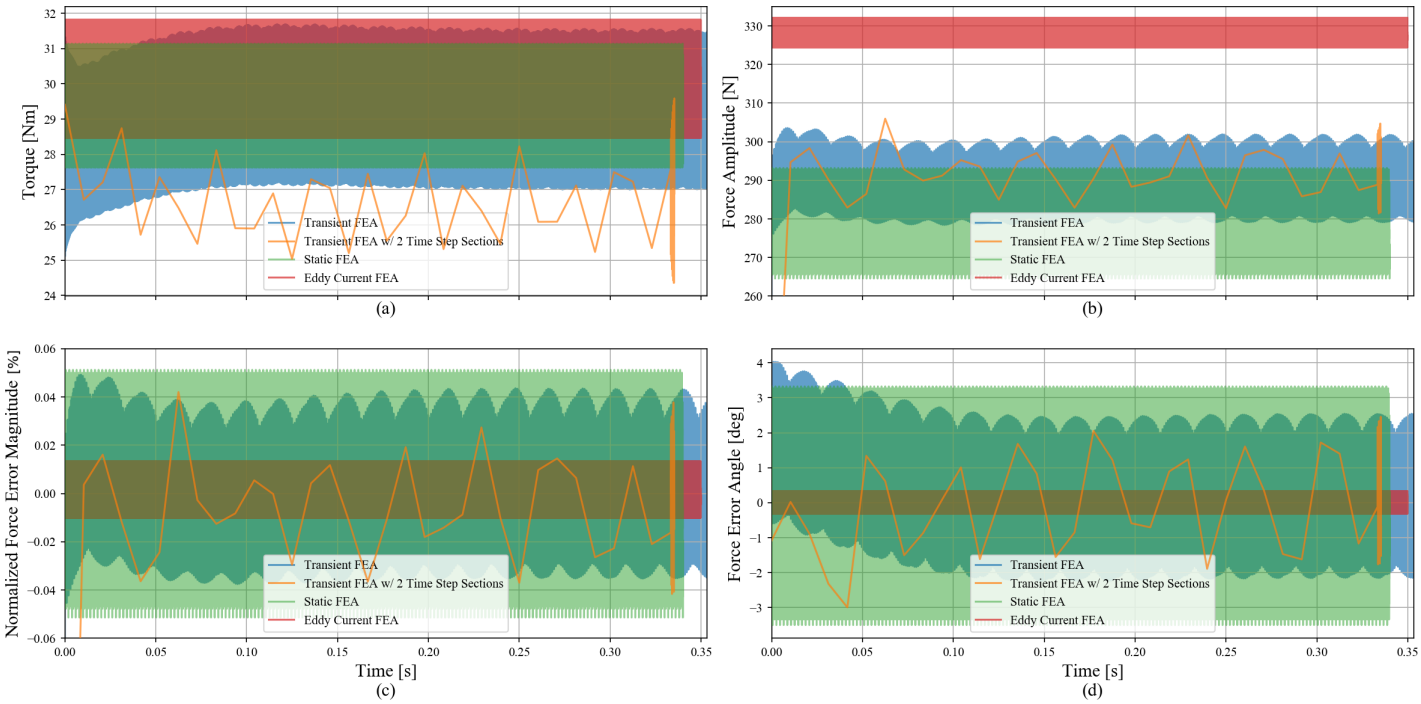

Fig. 5. FEA calulations of the models of Section IV for the example design developed in Section III: (a) torque; (b) force amplitude; (c) force error magnitude; and (d) force error angle. Force and torque results of eddy current FEA and static FEA are temporally extended for comparison with transient FEA.

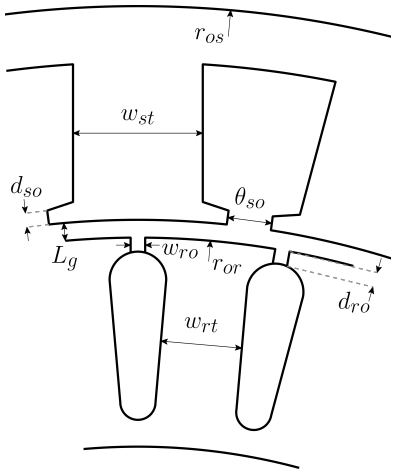

Fig. 6. Cross section view of the parameterized IM design.

B. Analysis of Example Design

The modelling techniques from Section IV are used to evaluate the example design of Fig. 1b. Results are shown in Fig. 5 and summarized in Table II. The eddy current FEA results (obtained over one rotor slot pitch–10 deg) and the static FEA results (obtained over 90 deg rotor rotation) are temporally extended for comparison purposes Fig. 5. Both transient solutions are initialized via an eddy current solution of the rotor bar currents, which nearly eliminates the start up transient in Fig. 5. The first portion of the "Transient FEA w/ 2 Time Step Sections" corresponds to a coarse time step (as described in Section IV-D), and the suddenly thick trace toward the simulation end time corresponds to when the fine time-step is used for performance metric calculations.

C. Analysis of Random Designs

An evaluation is conducted of 50 random bearingless IM designs. The designs are constructed by selecting random values for the geometry variables depicted in Fig. 6. The bounds of the variables are listed as follows: $L_g \in [0.5, 4]$ mm, $w_{st} \in [3, 9]$ mm, $\theta_{so} \in [1, 10]$ deg, $d_{so} \in [0.5, 3]$ mm, $w_{rt} \in [2.5, 6]$ mm, $w_{ro} \in [0.5, 3]$ mm, $d_{ro} \in [0.5, 3]$ mm. The stator and rotor outer radii are fixed as $r_{os} = 93.5$ mm and $r_{or} = 47.1$ mm, respectively.

The results are shown in Fig. 7 with their statistical data listed in Table III, where the accuracy of the design performance calculations is determined by comparing the values calculated by the three fast modeling methods to the reference transient FEA as described in Section V-A. Sensitivity of each technique to the solution's rotor position step size is indicated in Fig. 7 as three solution sets corresponding to a coarse, regular, and fine step size. For a transient solution, the rotor step size corresponds directly to the time-step size. For the static and eddy current modeling techniques, this corresponds to the increment size used for rotor position θ.

D. Analysis of Results

1) Simulation Time: The average time to evaluate a single candidate design for the proposed expedited transient FEA, the eddy current FEA, and the static FEA (with a regular solving step) are respectively 58 s, 40 s, and 33 s on a workstation PC with an Intel i7-7820X. Note that the static FEA model was solved with up to 5 parallel models.

2) Eddy Current FEA with Rotating Rotor: The eddy current solver yields inaccurate force and torque ripple calculations. Refinement of the step size does not appear to

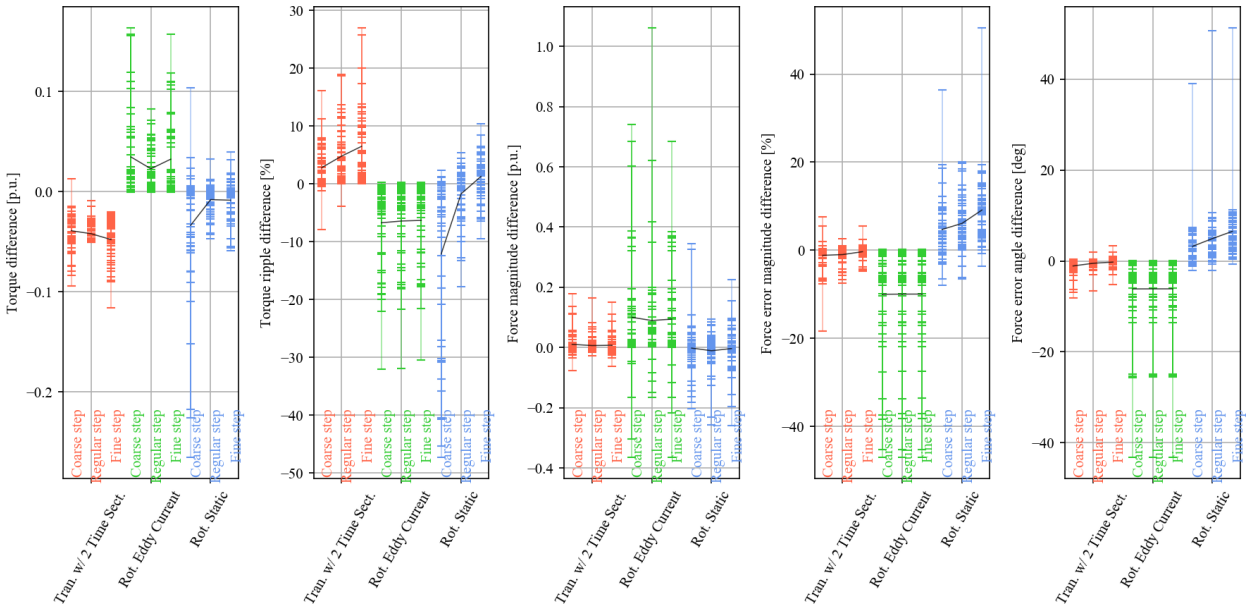

Fig. 7. Performance metrics compared against the reference transient FEA (see Section V-A). Each individual design is marked as a dash line '–'. Black lines connect study mean values with different solving steps. For transient FEA with two time-step sections, the solving steps for half the stator electric cycle are 16, 32 and 400. For eddy current FEA, the steps for one rotor slot pitch are 12, 24, 48. For static FEA, the steps for 90 mech. deg are 18, 45, 180.

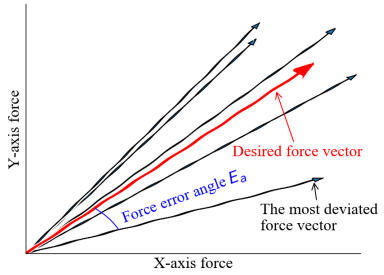

Fig. 8. Illustration of the definition of the force error angle.

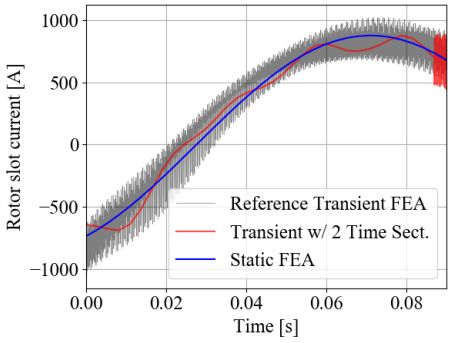

Fig. 9. Typical rotor slot current profiles of different FEA models.

increase the model accuracy, and Table III indicates that this modeling approach cannot be reasonably expected to accurately determine whether a design is within the 5° error angle calculation requirement mentioned earlier. A potential cause for the inaccuracies of the eddy current solution (and area for potential future improvement) may be how the eddy current solver accounts for magnetic saturation [46].

3) Static FEA with Pre-determined Rotor Currents: Static FEA is shown to be accurate for calculating the torque performance. However, like the eddy current method, the static FEA method is prone to inaccurate force ripple calculations, which are not improved through the use of a finer step size. One possible explanation for the inaccuracies is this approach's assumption of sinusoidal rotor slot currents. In reality these currents contain harmonics due to slotting, see Fig. 9.

4) Transient FEA with Two Time Step Sections: According to Table II and III, the proposed expedited transient FEA is able to accurately calculate both the force and torque performance, and the accuracy is statistically improved through refining solving step (Fig. 7). When considering the critical error angle E_a metric, this approach calculates E_a within $[-3.1, 2.0]$ deg for 49 out of 50 designs, while for the last design the E_a difference is -6.6 deg. This approach holds the most merit as a robust computationally efficient modeling tool for use in a design optimization.

VI. Conclusion

The first part of this paper discusses design considerations for bearingless IMs and investigates a design approach. Compared to regular IM, additional performance indices must be evaluated for the bearingless IM and the working principles of the IM make its evaluation different from bearingless permanent magnet machines. The second part of this paper proposes and evaluates computationally efficient FEA models of the bearingless IM. These techniques are shown to encompass a broad trade-off between calculation accuracy and computational expense. An expedited transient FEA model is proposed for use in machine optimization that exhibits high accuracy in the critical suspension force ripple calculations. Optimal design is considered as the future research.

References

[1] T. Hiromi, T. Katou, A. Chiba, M. A. Rahman, and T. Fukao, "A novel magnetic suspension-force compensation in bearingless induction-

motor drive with squirrel-cage rotor," *IEEE Transactions on Industry Applications*, vol. 43, no. 1, pp. 66–76, Jan 2007.

[2] M. Kang, "Research on multiphase bearingless motors (in chinese)," Ph.D. dissertation, Zhejiang University, 2008.

[3] A. Chiba, T. Fukao, and M. A. Rahman, "Vibration suppression of a flexible shaft with a simplified bearingless induction motor drive," *IEEE Transactions on Industry Applications*, vol. 44, no. 3, pp. 745–752, May 2008.

[4] A. Sinervo and A. Arkkio, "Rotor radial position control and its effect on the total efficiency of a bearingless induction motor with a cage rotor," *Magnetics, IEEE Transactions on*, vol. 50, no. 4, pp. 1–9, April 2014.

[5] A. Laiho, A. Sinervo, J. Orivuori, K. Tammi, A. Arkkio, and K. Zenger, "Attenuation of harmonic rotor vibration in a cage rotor induction machine by a self-bearing force actuator," *IEEE Transactions on Magnetics*, vol. 45, no. 12, pp. 5388–5398, 2009.

[6] A. Chiba, T. Fukao, O. Ichikawa, M. Oshima, M. Takemoto, and D. G. Dorrell, *Magnetic bearings and bearingless drives*. Elsevier, 2005.

[7] J. Asama, M. Amada, M. Takemoto, A. Chiba, T. Fukao, and A. Rahman, "Voltage characteristics of a consequent-pole bearingless pm motor with concentrated windings," *Magnetics, IEEE Transactions on*, vol. 45, no. 6, pp. 2823 –2826, june 2009.

[8] H. Mitterhofer, B. Mrak, and W. Gruber, "Comparison of high-speed bearingless drive topologies with combined windings," *IEEE Transactions on Industry Applications*, vol. 51, no. 3, pp. 2116–2122, 2015.

[9] D. Steinert, T. Nussbaumer, and J. W. Kolar, "Concept of a 150 krpm bearingless slotless disc drive with combined windings," in *Electric Machines & Drives Conference (IEMDC), 2013 IEEE International*. IEEE, 2013, pp. 311–318.

[10] J. Huang, B. Li, H. Jiang, and M. Kang, "Analysis and control of multiphase permanent-magnet bearingless motor with a single set of half-coiled winding," *IEEE Transactions on Industrial Electronics*, vol. 61, no. 7, pp. 3137–3145, 2014.

[11] T. Wang, J. Huang, B. Lin, M. Kang, J. Chen, and K. Wubin, "Eccentricity detection of a six phase induction motor with high frequency injection," *IET Electric Power Applications*, 2019.

[12] W. Khoo, "Bridge configured winding for polyphase self-bearing machines," *Magnetics, IEEE Trans on*, vol. 41, no. 4, pp. 1289–1295, 2005.

[13] W. Khoo, K. Kalita, and S. Garvey, "Practical implementation of the bridge configured winding for producing controllable transverse forces in electrical machines," *IEEE Trans on Mag.*, vol. 47, no. 6, 2011.

[14] E. Severson, R. Nilssen, T. Undeland, and N. Mohan, "Dual-purpose no-voltage winding design for the bearingless ac homopolar and consequent pole motors," *IEEE Transactions on Industry Applications*, vol. 51, no. 4, pp. 2884–2895, 2015.

[15] E. L. Severson, R. Nilssen, T. Undeland, and N. Mohan, "Design of dual purpose no-voltage combined windings for bearingless motors," *IEEE Transactions on Industry Applications*, vol. 53, no. 5, pp. 4368–4379, 2017.

[16] R. Oishi, S. Horima, H. Sugimoto, and A. Chiba, "A novel parallel motor winding structure for bearingless motors," *Magnetics, IEEE Transactions on*, vol. 49, no. 5, pp. 2287–2290, 2013.

[17] J. Huang, M. Kang, and J.-q. Yang, "Analysis of a new 5-phase bearingless induction motor," *Journal of Zhejiang University-SCIENCE A*, vol. 8, no. 8, pp. 1311–1319, 2007.

[18] M. Kang, J. Huang, J.-q. Yang, and H.-b. Jiang, "Analysis and experiment of a 6-phase bearingless induction motor," in *2008 International Conference on Electrical Machines and Systems*. IEEE, 2008, pp. 990–994.

[19] E. Severson, S. Gandikota, and N. Mohan, "Practical implementation of dual-purpose no-voltage drives for bearingless motors," *IEEE Transactions on Industry Applications*, vol. 52, no. 2, pp. 1509–1518, March 2016.

[20] R. S. Konwar, K. Kalita, A. Banerjee, and W. K. Khoo, "Electromagnetic analysis of a bridge configured winding cage induction machine using finite element method," *Progress In Electromagnetics Research B*, vol. 48, pp. 347–374, 2013.

[21] J. A. Santistebani, A. O. Salazar, and R. M. Stephan, "Modeling and analysis of a loaded bearingless machine," *EPE Journal*, vol. 10, no. 1, pp. 32–39, 2000.

[22] A. Chiba, "Transfer characteristics of radial force of induction-type bearingless motors with four-pole rotor circuits," *5th ISMB, 1996*, 1996.

[23] A. Chiba and T. Fukao, "Optimal design of rotor circuits in induction type bearingless motors," in *1998 IEEE International Magnetics Conference (INTERMAG)*, Jan 1998, pp. 225–225.

[24] A. Chiba and J. Asama, "Influence of rotor skew in induction type bearingless motor," *IEEE Transactions on Magnetics*, vol. 48, no. 11, pp. 4646–4649, 2012.

[25] J. M. S. Ferreira, M. Zucca, A. O. Salazar, and L. Donadio, "Analysis of a bearingless machine with divided windings," *IEEE Transactions on Magnetics*, vol. 41, no. 10, pp. 3931–3933, Oct 2005.

[26] X. Liu, T. Shi, L. Ding, X. Shao, and G. Xu, "Analysis of radial force and torque for bearingless wound-rotor induction motor," in *2011 International Conference on Electrical Machines and Systems*, Aug 2011, pp. 1–5.

[27] A. Chiba and J. Asama, "Influence of rotor skew in induction type bearingless motor," *IEEE Transactions on Magnetics*, vol. 48, no. 11, pp. 4646–4649, 2012.

[28] J. Pyrhonen, T. Jokinen, and V. Hrabovcova, *Design of rotating electrical machines*. John Wiley & Sons, 2013.

[29] Y. Duan, "Method for design and optimization of surface mount permanent magnet machines and induction machines," Ph.D. dissertation, Georgia Institute of Technology, 2010.

[30] Z. Zhao, S. Meng, C. Chan, and E. Lo, "A novel induction machine design suitable for inverter-driven variable speed systems," *IEEE transactions on energy conversion*, vol. 15, no. 4, pp. 413–420, 2000.

[31] Y. Kang and E. Severson, "Optimization framework for a large high speed bearingless permanent magnet motor," in *Sixteenth International Symposium on Magnetic Bearings*, 2018, pp. 1–10.

[32] Y. Kang and E. L. Severson, "Optimal design of 50kw concentrated winding bearingless motor," in *IEEE Energy Conversion Congress and Exposition (ECCE)*, 2018.

[33] K. Campbell, "High-speed induction motor with an integrated gearbox for propulsion," Master's thesis, 2017.

[34] P. Ponomarev, "Elmer fem induction machine tutorial," pp. 1–95, May 2017.

[35] L. Zhao, J. Huang, J. Chen, and M. Ye, "A parallel speed and rotor time constant identification scheme for indirect field oriented induction motor drives," *IEEE Transactions on Power Electronics*, vol. 31, no. 9, pp. 6494–6503, Sept 2016.

[36] K. Bradley, H Guldemir, "The effect of rotor design on rotor slot harmonics in induction machines," *Electric Power Components and Systems*, vol. 29, no. 9, pp. 771–788, 2001.

[37] T. A. Lipo, *Introduction to AC machine design*. John Wiley & Sons, 2017, vol. 63.

[38] D. Gerada, A. Mebarki, N. L. Brown, K. J. Bradley, and C. Gerada, "Design aspects of high-speed high-power-density laminated-rotor induction machines," *IEEE Transactions on Industrial Electronics*, vol. 58, no. 9, pp. 4039–4047, 2011.

[39] M. Amrhein and P. T. Krein, "Rotor designs for small inverter-dedicated induction machines," in *IEEE International Electric Machines and Drives Conference, 2003. IEMDC'03.*, vol. 2, June 2003, pp. 1279–1285 vol.2.

[40] V. F. Victor, F. O. Quintaes, J. S. Lopes, L. d. S. Junior, A. S. Lock, and A. O. Salazar, "Analysis and study of a bearingless ac motor type divided winding, based on a conventional squirrel cage induction motor," *IEEE Transactions on Magnetics*, vol. 48, no. 11, pp. 3571–3574, 2012.

[41] A. Chiba and T. Fukao, "Optimal design of rotor circuits in induction type bearingless motors," *IEEE Transactions on Magnetics*, vol. 34, no. 4, pp. 2108–2110, 1998.

[42] JMAG, "Transition to steady state in a short time," *JMAG White Papers*, 2017.

[43] D. Lin, P. Zhou, N. Chen, C. Lu, and M. Christini, "Fast methods for reaching ac steady state in fe transient analysis," in *Electric Machines and Drives Conference (IEMDC), 2017 IEEE International*. IEEE, 2017, pp. 1–6.

[44] A. Stermecki, O. Bíró, K. Preis, S. Rainer, and G. Ofner, "Numerical analysis of steady-state operation of three-phase induction machines by an approximate frequency domain technique," *e & i Elektrotechnik und Informationstechnik*, vol. 128, no. 3, pp. 81–85, 2011.

[45] M. Rosu, P. Zhou, D. Lin, D. M. Ionel, M. Popescu, F. Blaabjerg, V. Rallabandi, and D. Staton, *Multiphysics Simulation by Design for Electrical Machines, Power Electronics and Drives*. John Wiley & Sons, 2017, vol. 66.

[46] D. Meeker, "Finite element method magnetics," *FEMM*, 2010.